ADVANCED MATERIALS
www.advmat.d

Efficient Energy Funneling in Quasi-2D Perovskites: From Light Emission to Lasing

*Lei Lei, Dovletgeldi Seyitliyev, Samuel Stuard, Juliana Mendes, Qi Dong, Xiangyu Fu, Yi-An Chen, Siliang He, Xueping Yi, Liping Zhu, Chih-Hao Chang, Harald Ade, Kenan Gundogdu, and Franky So**

Quasi-2D Ruddlesden–Popper halide perovskites with a large exciton binding energy, self-assembled quantum wells, and high quantum yield draw attention for optoelectronic device applications. Thin films of these quasi-2D perovskites consist of a mixture of domains having different dimensionality, allowing energy funneling from lower-dimensional nanosheets (high-bandgap domains) to 3D nanocrystals (low-bandgap domains). High-quality quasi-2D perovskite $(PEA)_2(FA)_3Pb_4Br_{13}$ films are fabricated by solution engineering. Grazing-incidence wide-angle X-ray scattering measurements are conducted to study the crystal orientation, and transient absorption spectroscopy measurements are conducted to study the charge-carrier dynamics. These data show that highly oriented 2D crystal films have a faster energy transfer from the high-bandgap domains to the low-bandgap domains (<0.5 ps) compared to the randomly oriented films. High-performance light-emitting diodes can be realized with these highly oriented 2D films. Finally, amplified spontaneous emission with a low threshold 4.16 µJ cm^{-2} is achieved and distributed feedback lasers are also demonstrated. These results show that it is important to control the morphology of the quasi-2D films to achieve efficient energy transfer, which is a critical requirement for light-emitting devices.

Organometal halide perovskites have attracted tremendous attention as the next-generation semiconducting materials for optoelectronic devices.[1–3] Specifically, owing to their favorable optical and electrical properties such as high carrier mobility, high photoluminescence quantum yield (PLQY), wide wavelength tunability, and high color purity,[4–6] they have been attractive for light-emitting diode (LED) applications. Since the first demonstration of perovskite LEDs in 2014,[7] the device external quantum efficiency (EQE) has risen rapidly from 0.1%[7] to ≈20%,[2,4,8] and the efficiency enhancements are mainly attributed to passivation and compositional engineering,[2,8] improved charge balance by optimization of device structure,[9] and efficient light extraction.[4] More recently, these materials are considered as optical gain medium for lasers. In 2014, the first amplified spontaneous emission (ASE) was observed from $CH_3NH_3PbI_3$ thin films with a threshold of 12 µJ cm^{-2} and a gain of 250 cm^{-1}, which is ascribed to the large absorption coefficient, low bulk defect density, and slow Auger recombination rate.[10] These ASE threshold and gain values are comparable to the state of art gain media such as colloidal quantum dots[11] and organic thin films.[12] Since then, optically pumped lasers have been demonstrated based on various microcavity structures such as Fabry–Pérot cavities,[13,14] distributed feedback (DFB) gratings,[3,15] and whispering gallery cavities.[16] The flexibility of fabricating hybrid perovskite lasers using solution-processed methods enables large-scale production and is attractive for the realization of on-chip integration of photonic circuits.[17]

Quasi-2D perovskites, which are also known as Ruddlesden–Popper (RP) perovskites, are mixed phases of 2D and 3D nanocrystals. In the mixture, 2D domains exhibit quantum-well-like electronic properties with strong exciton binding energy due to the reduced dimensionality.[18] Typically, the 2D perovskite $(A')_2A_{n-1}B_nX_{3n+1}$ domains consist of multilayers of BX_6 octahedra separated by intercalating ammonium cations A', which is too large to fit into the crystal structure and hinder the growth of 3D ABX_3 crystals (A = methylammonium (MA$^+$), formamidinium (FA$^+$), or Cs$^+$, B = Pb^{2+}, and X = I$^-$, Br$^-$, Cl$^-$). As a result, the number of layers determine the bandgap of 2D quantum-well-like domains.[19] Different from 3D perovskites, thin films of qausi-2D perovskites typically contain a mixture of domains with different layers. Within such inhomogenous

---

L. Lei, J. Mendes, Q. Dong, Dr. X. Fu, S. He, Dr. X. Yi, Dr. L. Zhu, Prof. F. So
Department of Materials Science and Engineering
Organic and Carbon Electronics Lab (ORaCEL)
North Carolina State University
Raleigh, NC 27695, USA
E-mail: fso@ncsu.edu

D. Seyitliyev, S. Stuard, Prof. H. Ade, Prof. K. Gundogdu
Department of Physics
Organic and Carbon Electronics Lab (ORaCEL)
North Carolina State University
Raleigh, NC 27695, USA

Y.-A. Chen, Prof. C.-H. Chang
Department of Mechanical and Aerospace Engineering
North Carolina State University
Raleigh, NC 27695, USA

The ORCID identification number(s) for the author(s) of this article can be found under https://doi.org/10.1002/adma.201906571.

DOI: 10.1002/adma.201906571

domain distribution, it is assumed that the energy rapidly funnels from the high-bandgap domains (donors) to the low-bandgap domains (acceptors) and finally it emits radiatively in the high-dimensional domains.[20] This process results in rapid charge-carrier localization and increased carrier concentration in acceptors, which enhances the bimolecular recombination rate,[21] as well as facilitates the build-up of population inversion.[22] Therefore, it makes quasi-2D perovskites promising for both LED and lasing applications. For example, the LEDs based on quasi-2D perovskites recently demonstrated EQE exceeding 15% with PLQY of 70%.[23] Moreover, the outstanding low ASE threshold of 8.5 µJ cm^{-2} in 1-naphthylmethylammonium (NMA = $C_{10}H_7CH_2NH_3^+$)-based quasi-2D perovskites was first demonstrated last year.[22] Since then, there have been several reports on ASE and lasing in quasi-2D perovskite materials.[24–26] It is demonstrated that a graded domain distribution is favorable for efficient energy funneling,[27,28] in which the amount of low-bandgap acceptors is larger than the high-bandgap donors. Thus, it is able to achieve high quantum yield as well as enhanced LED performance. However, a consensus about how the morphology such as nanocrystal orientation affects the energy transfer process is still lacking. For example, it was reported that thin films with randomly oriented crystals exhibit more efficient charge transport and improved radiative recombination compared to that of thin films with parallel oriented domains in LEDs,[29] and the authors explained that the insulating organic layer hindered the charge transfer due to the parallel oriented nanocrystal structure. On the other hand, when ASE is compared, the thin films with preferred oriented crystals exhibited a lower ASE threshold.[30] In contrast, randomly oriented nanocrystals either exhibited ASE at much higher thresholds or did not exhibit any ASE,[30] indicating a more efficient energy funneling in thin films with preferential orientation. So far, the impact of morphology on the energy transfer dynamics remains ambiguous. In order to achieve high-quality optoelectronic perovskite devices, it is essential to understand the role of morphology in charge and energy transfer kinetics as well as to develop methods to control the morphology of the thin films.

In this work, we demonstrate one-step solution-processed phenethylamine (PEA)-based quasi-2D, multi-phasic perovskite thin films with a highly efficient energy transfer rate from the 2D phase to the 3D phase. In our work, we observed that the efficiency of energy transfer is largely influenced by the nanocrystal orientation, which can be efficiently tuned using different precursor solvents. Via solvent engineering, a high quality of quasi-2D perovskite films with preferential orientation is achieved, resulting in a significant improvement in PL intensity. The texture of these quasi-2D perovskite thin films was studied with grazing-incidence wide-angle X-ray scattering (GIWAXS). The dynamics of energy transfer was studied by time-resolved absorption spectroscopy (TAS), revealing a more efficient energy funneling process in the well-oriented thin films. We propose that highly oriented domains are beneficial for efficient energy funneling from high-bandgap domains to low-bandgap domains due to the alignment of the in-plane transition dipole moments, facilitating an efficient Förster energy transfer. As a result, the optimized LED device based on these quasi-2D films resulted in a high current efficiency of 41 cd A^{-1} and EQE of 11.5%. The same thin films also exhibit a very low ASE threshold of 4.16 µJ cm^{-2}. Based on these findings, we further demonstrate optically pumped DFB lasers with a low threshold. Our results show that it is important to control the texture of the quasi-2D films to achieve efficient energy transfer, which is critical for optoelectronic devices.

The quasi-2D RP-layered perovskites used in this study were fabricated by spin-coating the precursors, which consist of phenethylammonium bromide (PEABr), formamidinium bromide (FABr), and lead bromide ($PbBr_2$) with a molar ratio of 2:3:4. Since the dimensionality of RP-phase perovskites can be tuned by adjusting the composition of precursor solutions, here we focus on the stoichiometry of $n = 4$ $(PEA)_2(FA)_3Pb_4Br_{13}$ unless otherwise stated. During the spin-coating process, a small amount of antisolvent (chlorobenzene) was dripped onto the thin films, inducing rapid supersaturation and immediate crystallization.[31] In order to tune the morphology of perovskite thin films, different precursor solvents are used since it is considered as an effective way to utilize the solution-based intermediate phase by adjusting the activation energy and growth kinetics,[32] which is largely affected by the solvent properties such as donor number indicating the coordinating ability of the Lewis-basic solvents with the Lewis acidic Pb^{2+} center[33] and evaporation rate.[34] In this work, *N*-methyl-2-pyrrolidone (NMP) and dimethyl sulfoxide (DMSO) are chosen as the precursor solvents since they both can be used as a Lewis base to form the intermediate phase with lead halides, which results in high-quality perovskite films.[33] However, the differences in the evaporation rate, surface wettability, and interaction with organic cations between DMSO and NMP might lead to the difference in crystal size and the resulting morphology of quasi-2D perovskite thin films.[34–36]

To study the structure of the films, GIWAXS measurements were done to determine the crystal structure as well as the texture of these perovskite films. As shown in **Figure 1**, the GIWAXS data from an incident angle of 1° show the differences

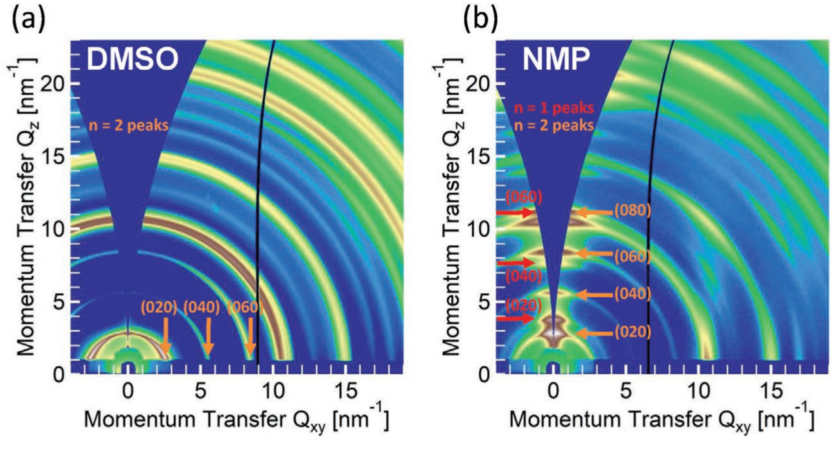

Figure 1. a,b) GIWAXS patterns of the spin-cast perovskite films from solvent DMSO (a) and NMP (b). Unique peaks from an $n = 2$ layered perovskite phase are indicated by orange indices/arrows, while those from $n = 1$ are in red.

between the two thin films. The film made by DMSO shows long arcs of intensity in the GIWAXS pattern indicating that the crystallites are isotropically distributed without any preferred orientation.[37] In contrast, the pattern from the NMP film displays sharp peaks with short arc lengths along the Q_z-axis. These scattering points are indicative of a strongly textured, preferentially oriented film. Previous work showed that thin films of stoichiometric $n = 4$ layered perovskites contain mixed phases of $n = 1, 2, 3$ layered perovskite as well as the corresponding 3D phase, such as (FA)PbI_3.[38] Because of the large spacing (created by organic spacer molecules like PEA) between the strong scattering lead-iodide layers in layered perovskites, only layered perovskite phases (and not the bulk phase) can generate scattering momentum transfers less than 10 nm^{-1} (since there is an inverse relationship between real spacing and reciprocal spacing).[39] In the present DMSO pattern, three scattering signatures at less than 10 nm^{-1} are noticeable. Using indexGIXS software to fit these low-Q peaks to the expected scattering from several potential-layered perovskite unit cells, the three peaks were identified as being generated from the family of (0k0) planes in the $n = 2$ layered perovskite.[40] As seen in the pattern, the arc from the diffraction signal is close to isotropic, indicating that the lead-bromide sheets of $n = 2$ oriented randomly having a slightly perpendicular ("edge-on") orientation in the films. The $n = 2$ scattering signal is also present in the NMP sample, but in a very different way. As clearly indicated on the pattern, the same (0k0) family of peaks is now shown on the Q_z-axis. The sharp intensity of these peaks as well as the short arc length means that the lead-bromide sheets in this sample are parallel to the substrate. Similarly, an $n = 1$ (0k0) family of peaks is also present in the in-plane orientation. There are not many differences between the GIWAXS data from different incident angles of 0.15° (Figure S1, Supporting Information) and 1°, indicating good uniformity of nanostructures along the vertical direction of the films. These observations are consistent with the X-ray diffraction (XRD) patterns (Figure S2, Supporting Information). A family of (0k0) planes in $n = 1$ and $n = 2$ layered perovskites is clearly observed in the NMP film. In contrast, very weak peak intensity is observed in the $n = 2$ layered DMSO perovskite sample. Moreover, compared to the film made from DMSO, a broader peak at 14.9° in the NMP film indicates the reduction of 3D nanocrystal size, which promotes bimolecular radiative recombination.[6] The surface morphology of the perovskite thin films is observed by scanning electronic microscopy (SEM) and atomic force microscopy (AFM). As shown in the SEM images (Figure S3, Supporting Information), thin films with uniform surface coverage are obtained for all samples. Fewer features are present in the film made with the NMP solvent than the DMSO solvent, indicating a smoother surface. AFM measurements (Figure S4, Supporting Information) also confirm that a decrease of roughness is observed in the NMP sample compared to the DMSO sample.

The optical properties of quasi-2D perovskites are largely affected by the texture and morphology. Figure S5a (Supporting Information) shows the UV–vis spectra for thin films prepared by DMSO and NMP. According to previous reports of $PbBr_4$-based quasi-2D perovskites, the absorption peaks at 401 and 434 nm are assigned to the $n = 1$ and $n = 2$ domains,[29,41] respectively, due to the quantum confinement effects.[5] The absorbance spectra of the quasi-2D perovskite film prepared by the DMSO solvent show a strong absorption peak at 434 nm, indicating that the major component of the perovskite film is the $n = 2$ domains. The weak absorption peak at 460 nm shows the existence of the $n = 3$ domains, and the presence of the $n = 1$ domains is almost negligible. However, in the NMP film, the relatively even and small excitonic absorption peaks at 401 and 434 nm indicate a similar fraction of the $n = 1$ and $n = 2$ domains. The signals for $n \geq 4$ domains are not visible in the absorption spectrum. For both samples, the band edge absorption of 3D domains appears as shoulders at around 530 nm, indicating a mixture of 2D and 3D domains. The PL spectra for the perovskite films prepared by different solvents are plotted in Figure S5b (Supporting Information). It is clear that a stronger emission is observed in the perovskite film prepared using NMP, indicating reduced nonradiative recombination centers. It is worth mentioning that a slight blue-shift of emission peak is observed in the NMP sample, which is consistent with the XRD data indicating a reduction of the crystal size in the 3D domains.

We further carried out ultrafast TAS measurements to get a deeper insight into the transfer dynamics of photocarriers and thereby reveal the difference between the two quasi-2D films prepared by NMP and DMSO. The representative 2D maps of the transient absorption spectra with an excitation wavelength of 355 nm are shown in Figure S6 (Supporting Information). Here, the change in transmittance is showed as a color heightmap as a function of wavelength and pump delay. We further extract the evolution of the transient absorption spectra at early time delays as shown in **Figure 2**a,b. Several bleaching features are present, and the decay kinetics coincide with the features of energy transfer reported previously.[20] For both NMP and DMSO films, the initial photoexcitation is formed on the low-dimensional domains, evidenced by the ground state bleaching (GSB) feature at ≈430 nm, which is in agreement with the peak position of $n = 2$ domain from the steady-state absorption spectrum (Figure S5a, Supporting Information). The bleaching features at lower energy can be assigned as the GSB signals of higher dimensional perovskite domains, and the corresponding n values are marked. Upon excitation, the photoexcited carrier population in the high-dimensional domains rises as the population decays in the low-dimensional domains, indicating the energy funneling from the high-bandgap domains to the lower-bandgap 3D domains. In both thin films, the $n = 2$ domain population decays in < 1 ps initially with the remaining bleaching signal lasting for a long time period (≈1000 ps). This suggests that charge carriers are accumulated in the $n = 2$ domains and the energy transfer is incomplete which is supported by the time-resolved PL (TRPL) decays at 440 nm in Figure S7a (Supporting Information). However, by comparing spectral line shapes in Figure 2a,b for the DMSO and NMP samples, it clearly shows a larger population of carriers remaining in the 2D domains for the DMSO indicating an incomplete energy transfer. Extracting the domain distribution information from the absorbance spectra and TAS data, we conclude that the acceptor (3D domains) to donor (2D domains) ratio is larger in the NMP film than the DMSO film. This higher acceptor concentration could be the reason for more complete and efficient

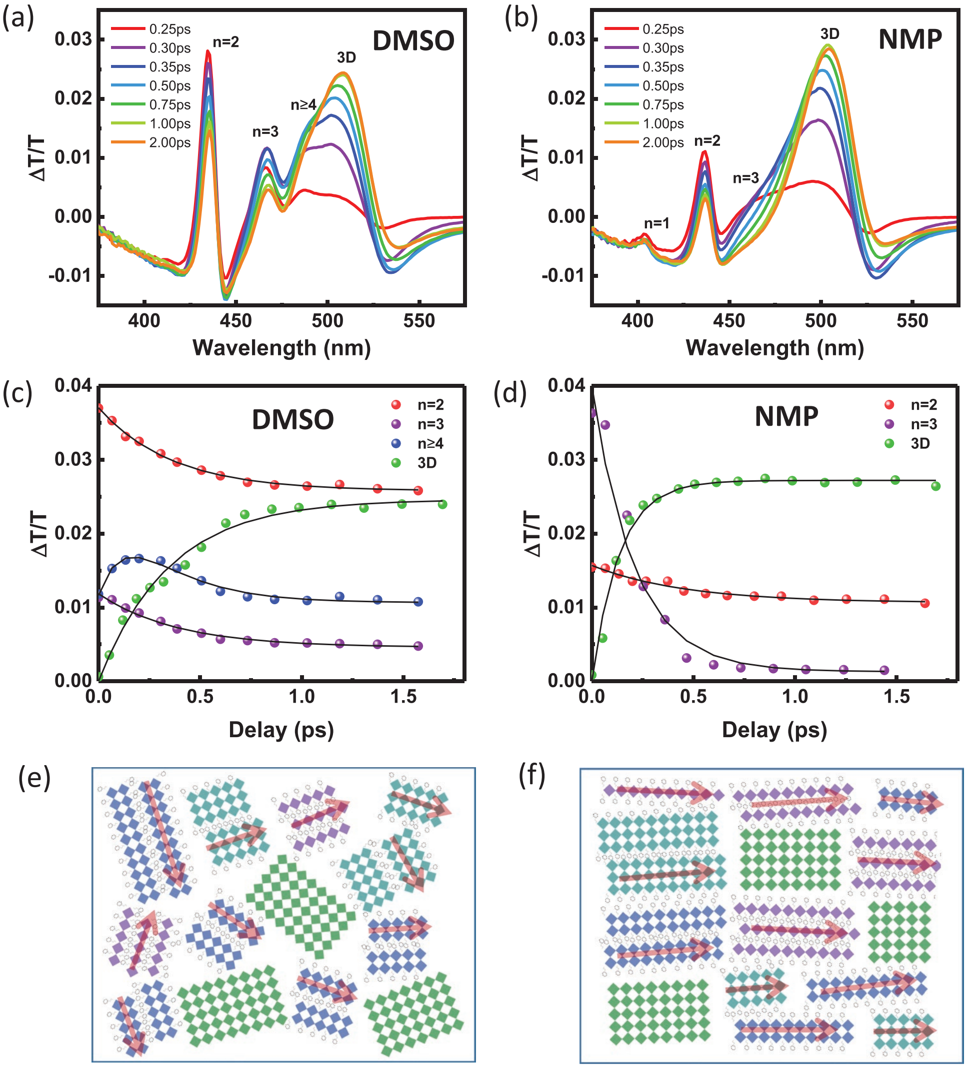

Figure 2. a,b) Transient absorption spectra at various delay times of the perovskite films from solvent DMSO (a) and NMP (b), and c,d) de-convolved dynamics of photobleaching features at $n = 2$, $n = 3$, $n \geq 4$ and 3D phases for DMSO (c) and NMP (d) samples. The black curves represent the best fit obtained for the corresponding dynamics. e,f) Schematic of illustrations of quasi-2D perovskite with random orientation (e) and preferential orientation (f). The arrows indicate the transition dipole orientation in nanocrystals.

energy transfer due to less trapped population in the NMP film.[27,28]

In order to further study the energy transfer dynamics from the higher energy domains to the lower energy 3D perovskite domains, we de-convolved the spectra and plotted the evolution of each domain signal as a function of time in Figure 2c,d. The fitting of the dynamics of photobleaching at different wavelengths is shown in Figure 2c,d, and the results are summarized in Table S1 (Supporting Information). In the DMSO sample, upon the initial excitation, the population in the $n = 2$ and $n = 3$ domains showed a relaxation with a similar decay time constant (≈0.3 ps), and the $n \geq 4$ domains showed a faster rise time (0.2 ps) indicating a built-up of photocarriers followed by a slower decay (0.4 ps). In addition, the rise time for the 3D domains is 0.36 ps, which further supports the accumulation of excitons in the 3D domains is dominated by the energy transfer from the high-bandgap domains (low n-value phase) to the low-bandgap domains (3D perovskites) within the same timescale.[20] The data show a similar trend for the thin film made from NMP, whereas the $n \geq 4$ domains are not visible in the TAS signal. It should be noted that the rising time of the 3D domain is about 0.13 ps for the NMP sample, which is significantly faster than the 3D domain dynamics observed (0.36 ps) for the DMSO sample, indicating that photocarriers relaxed to the 3D domain in the NMP sample are faster than that in the DMSO sample. This fast exciton capture time in the 3D domains for the NMP sample within 0.13 ps is faster than the 10–100 ps energy transfer rate reported previously,[5,20] suggesting that this faster energy transfer rate is due to the highly oriented nanocrystal structures provided by the NMP solvent. Energy transfer can happen as a radiative transfer or nonradiative transfer such as Förster resonance energy transfer (FRET) and Dexter exchange energy transfer from a donor to an acceptor.[42] Since the thickness of the insulating intercalating organic layer is larger than 1 nm,[43] the energy transfer from the 2D to the 3D domains is more likely due to FRET, which depends on the overlap of the donor emission and acceptor absorption spectra, the transition dipole orientation and the donor–acceptor separation.[28,44–46] In the NMP sample, oriented crystal gives a higher density,[30] along with a smaller spacing between the domains. Thus, the decreased donor–acceptor spacing gives rise to a higher energy transfer efficiency. Moreover, the band structure calculations have predicted that the transition dipole moments are inclined to orient along the nanosheet direction in 2D perovskites,[47] which also have been confirmed by the anisotropic exciton response observed experimentally.[43,48] Therefore, it is proposed that the highly oriented low-dimensional domains in the NMP samples give a preferential transition dipole orientation (mostly parallel to the substrate), which also makes the energy transfer more efficient.[44] Hence, we hypothesize that the quasi-2D perovskites films introduced by NMP solvent with a faster energy transfer are caused by enhanced FRET efficiency due to the decreased donor–acceptor distance and the aligned dipole orientation between crystals. The schematic of the proposed mechanism is shown in Figure 2e,f.

To demonstrate the importance of efficient energy transfer from the quasi-2D domains to the 3D domains, LEDs were fabricated using on these quasi-2D perovskite films. A device structure of indium tin oxide (ITO)/nickel oxide (NiO_x)/poly(vinylpyrrolidone) (PVP)/quasi-2D perovskites/2′,2′-(1,3,5-benzinetriyl)-*tris*(1-phenyl-1-*H*-benzimidazole) (TPBi)/Cs_2CO_3/Al is used and the schematic diagram is shown in the inset of **Figure 3**a. Here, an ultrathin layer of PVP is used to passivate the surface of NiO_x in order to suppress the exciton quenching as previously reported.[49] The current density–voltage–luminescence and the current efficiency–current density characteristics are plotted in Figure 3a,b, respectively. From the current density versus voltage (*J*–*V*) curves, a slight decrease of the current density is observed at voltages above 4 V for the device having a perovskite layer using NMP as a solvent. This decrease in current density may be due to the insulating organic layer parallel to the substrate-impeding charge transport. On the other hand, there is no significant difference in the turn-on voltage (3 V) in devices with films processed using both solvents indicating that the parallel-oriented quasi-2D perovskite films does not affect carrier injection. However, the LED devices based on the NMP film yield a higher luminescence at 7 V (Figure 3a) and an enhanced current efficiency (CE; Figure 3b) due to the faster radiative recombination rate via more efficient energy transfer. The devices with two different solvents give the same electroluminescence (EL) peaks at 525 nm as shown in the inset of Figure 3b. Both devices show good repeatability, as EQE histogram among ≈25 devices as shown in Figure S8 (Supporting Information). The best performing device with the DMSO film yields a CE of 32 cd A^{-1}, while an LED device with NMP processed film shows as high as 41 cd A^{-1} resulting in an EQE of 11.5%. This efficiency enhancement is attributed to the high quality of the quasi-2D perovskite film with a smooth surface, high crystallinity, as well as highly oriented nanocrystals, which gives a more efficient energy transfer and radiative recombination.

To investigate whether an efficient energy transfer between the domains leads to low ASE threshold, we use a 150 fs pulse laser having a repetition rate of 1 kHz to excite the quasi-2D perovskite thin films on quartz substrate. The laser excitation wavelength is 400 nm and the excitation spot is 4.5 mm in diameter. **Figure 4**a,b shows the pump fluence–dependent PL spectra for films prepared from DMSO and NMP solvents, respectively. At low pump fluences, the spontaneous emission (SE) spectrum is centered at 537 nm with a full-width at half-maximum (FWHM) of 28 nm. When the pump fluence exceeds the ASE threshold, a narrower bandwidth (≈4 nm) ASE peak appears at 542 nm. In the intensity–pump fluence plot, the ASE threshold is represented as a sharp increase in the slope. The ASE threshold of the NMP sample (4.16 μJ cm^{-2}) is one order lower than that of the DMSO sample (51.08 μJ cm^{-2}) and the data are shown in Figure 4c,d. To determine the threshold carrier density *N*, the equation is used: $N = \alpha \frac{P\lambda}{hc}$.[22] Here, *P* is the measured ASE threshold power fluence, λ is the excitation wavelength, *h* is the Planck's constant, *c* is the light speed in vacuum, and α is the absorption coefficient (for the DMSO sample, $\alpha = 1.4 \times 10^5$ cm^{-1} and for the NMP sample, $\alpha = 1.7 \times 10^5$ cm^{-1} at 400 nm from the UV–vis measurements). As a result, the threshold carrier density for the DMSO sample is determined to be 1.5×10^{19} cm^{-3}, one order of magnitude higher than the NMP sample at 1.4×10^{18} cm^{-3}. By comparing the TRPL decays for both DMSO and NMP samples in Figure S7 (Supporting Information), no significant difference of PL lifetime is observed, suggesting that the defect passivation effect is not obvious in the NMP sample. Therefore, the lower threshold in the NMP sample is attributed to a faster energy

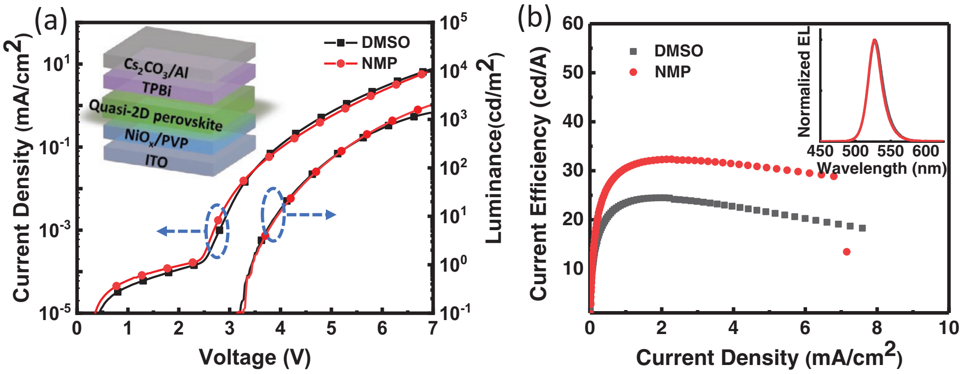

Figure 3. Device performance of PeLEDs. a) *J*–*V*–*L* data (inset shows the device structure), b) current efficiency (EL shown in the inset) of the devices based on perovskite films prepared from NMP and DMSO solvents, respectively.

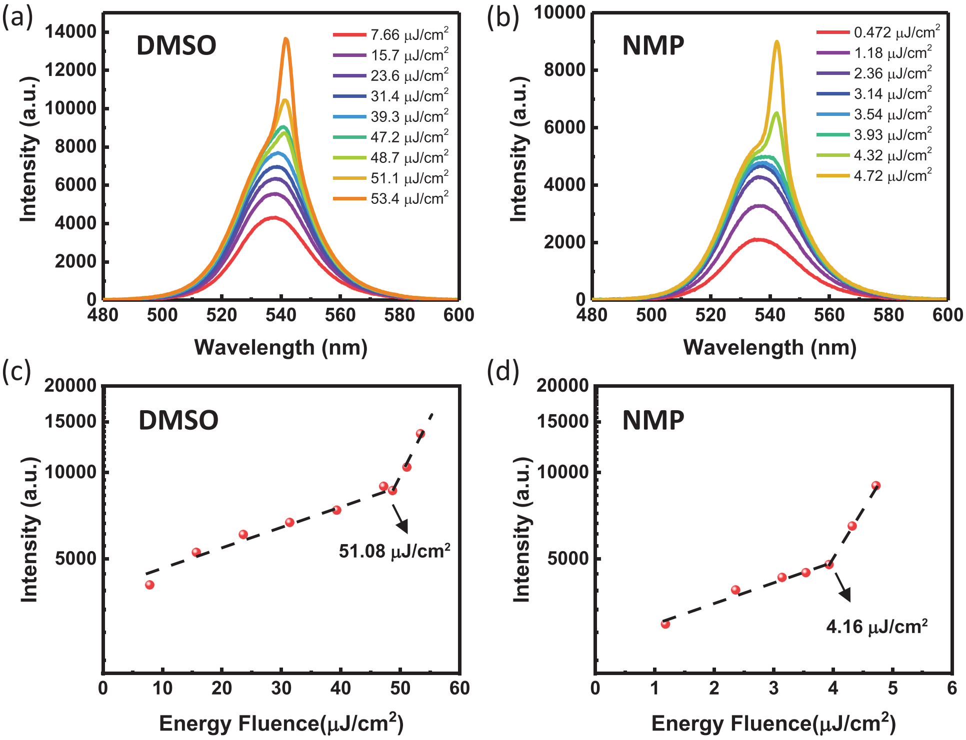

Figure 4. ASE for quasi-2D perovskite thin films. a,b) Pump-fluence dependence of the emission on perovskite thin films prepared from DMSO (a) and NMP (b) with the excitation laser (400 nm, 150 fs pulses), respectively. c,d) ASE threshold is measured by PL intensity versus pump fluence at ASE peak (≈542 nm) for DMSO (c) and NMP (d) samples, where DMSO shows threshold of 51.08 μJ cm^{-2} and NMP shows threshold of 4.16 μJ cm^{-2}.

funneling process than the DMSO sample, leading to a faster population inversion build-up in the low-bandgap domains.[22]

The lower threshold carrier density for the NMP sample indicates a possibility of attaining a gain from optical pumping.[10] To demonstrate lasing in the low ASE threshold quasi-2D perovskite thin film processed with the NMP solvent by optical pumping, a DFB laser having a 1D grating (period $\Lambda = 350$ nm) was fabricated. To fabricate a DFB laser, the grating substrate was fabricated by interference lithography (IL) and nanoimprinting, followed by spin coating of a 100 nm thick layer of spin-coated perovskite on the grating. Note the grating has relatively large features and low aspect ratio compare with the nanocrystals and is not expected to change the morphology of the perovskite films. The SEM cross-section of the DFB laser is shown in **Figure 5**a. The perovskite film thickness is chosen to support only the fundamental transverse electric (TE_0) waveguide mode. While the second-order Bragg diffraction of the grating creates the optical resonance at the ASE wavelength, the first-order Bragg diffraction diffracts the waveguide mode into the surface normal as the laser output.[50] The sample was optically pumped at room temperature using the same pulsed optical pumping as the ASE setup. As the pump fluence increases, a clear emission power threshold is observed at 10 μJ cm^{-2} (Figure 5b). Above the threshold, we observe the lasing emission with the line-narrowing (FWHM of 1.7 nm, as shown in Figure 5c) and a linear laser emission pattern corresponding to the width of the excitation spot (Figure 5b inset). The lasing emission is strongly TE polarized, which is consistent with the characteristics of the DFB lasers,[51] demonstrating a green DFB laser having a low threshold and good spatial coherence using oriented crystal perovskite thin films. Further improvements need to be done to enhance the perovskite emission characteristics by optimizing the grating structure.[15]

In summary, we demonstrate quasi-2D RP perovskite films prepared via a simple solution process which exhibits desirable optical properties for high-efficiency LEDs and low ASE threshold. The perovskite nanocrystal orientation is strongly affected by different precursor solvents, DMSO and NMP. By using NMP as precursor solvent, quasi-2D perovskite crystals with a strong preferred orientation can be achieved, while the DMSO solvent results quasi-2D perovskite crystals with random orientation. These highly oriented perovskite films show a more efficient energy transfer due to the preferred transition dipole orientation and decreased donor–acceptor distance. This understanding of perovskite nanocrystal orientation sheds light on the requirements for light-emitting devices. Using the optimized quasi-2D perovskite films, we demonstrated a high-efficiency LED device with a CE of 41 cd A^{-1}, corresponding to an EQE of 11.5%. We further demonstrate a low ASE threshold of 4.16 μJ cm^{-2} and a green emission DFB laser based on the optimized perovskite thin films. Our results demonstrate an effective method to obtain good-quality quasi-2D, multiphasic perovskite thin films for LED and laser applications.

Experimental Section

Material Preparation: The $(PEA)_2(FA)_3Pb_4Br_{13}$ precursors were prepared by dissolving PEABr, FABr, $PbBr_2$ (2:3:4 molar ratio) and MACl (0.05 mmol) in 1 mL anhydrous NMP or DMSO solvent to make

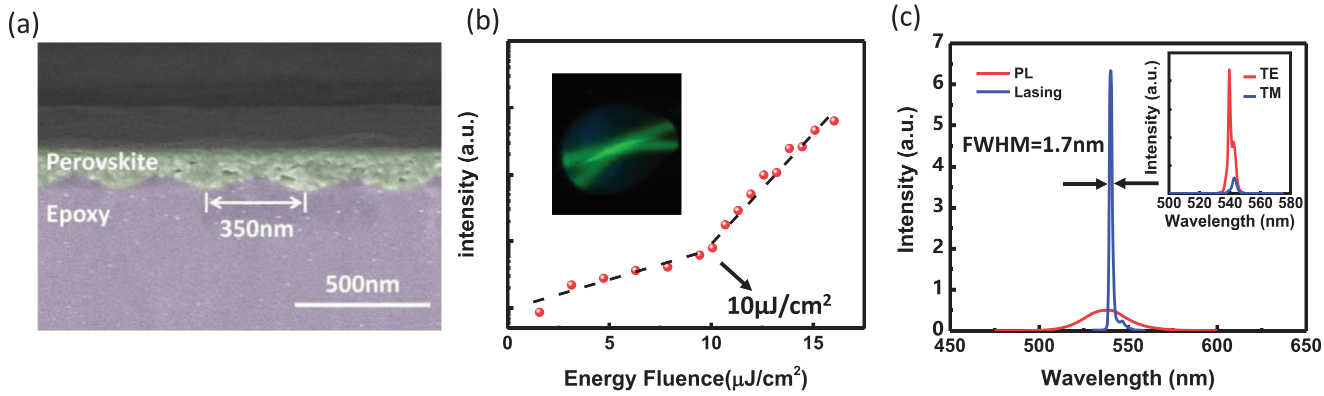

Figure 5. DFB laser based on quasi-2D perovskites thin films with well-oriented domains. a) SEM cross-section of DFB lasers with a period of 350 nm and quasi-2D perovskite thin films with a thickness of 100 nm. b) Lasing threshold measurement of DFB laser. The inset is the photograph of far-field lasing emission projected on white paper. c) PL emission measured from the planar thin film and lasing emission measured from the surface of device containing DFB gratings pumped with 400 nm 150 fs laser. The polarization of lasing emission is shown in the inset.

0.5 M (Pb^{2+} concentration) solutions. The solutions were stirred for 2 h at 60 °C in a glovebox with a nitrogen environment.

The NiO_x solution precursor was synthesized according to the previous publication.[49] Nickel acetate tetrahydrate ($Ni(CH_3COO)_2 \cdot 4H_2O$) and ethanolamine($NH_2CH_2CH_2OH$) were dissolved in ethanol (0.1 mol L^{-1}) with a molar ratio of 1:1, and stirred at 65 °C for 1 h.

Fabrication of Perovskite LEDs: The prepatterned ITO-coated glass substrates were used to fabricate the LEDs. First, the substrates were cleaned in acetone and isopropanol for 15 min in sequence, and then dried by N_2. The cleaned substrates were UV-ozone treated for 15 min. NiO_x as the hole injection layer was prepared by spin-coating NiO_x precursor at 2000 rpm for 40 s and baked at 500 °C for 1 h in ambient air. Then the substrates were transferred into a glovebox. An ultrathin passivation layer was spin-coated by PVP (4 mg mL^{-1}) in dimethylformamide at 5000 rpm for 30 s, and annealed at 120 °C for 10 min. Thereafter, the perovskite solution was spin-coated onto the NiO_x films at 3000 rpm for 2 min, during which time (at 28 s for DMSO and 31 s for NMP) chlorobenzene (150 μL) was dripped onto the surface, followed by annealing at 90 °C for 10 min. The as-prepared substrates were then transferred into a thermal evaporator, and 40 nm TPBi, 2 nm Cs_2CO_3, and 100 nm Al were deposited layer by layer. The device area was defined by the area of overlap of ITO anode and Al cathode 4 mm^2 (2 × 2 mm). Finally, the fabricated devices were sealed in glovebox by ultraviolet-curable resin before testing.

Fabrication of DFB Laser: The DFB cavity was fabricated by using nanoimprinting lithography from a silicon master nanostructure. The nanostructures on silicon molds were patterned using IL and transferred using reactive ion etching (RIE). First, a 100 nm antireflection coating (ARC) and 180 nm positive photoresist (PR) were spin-coated on silicon substrate. The ARC film was used to reduce the reflection from the substrate during lithography. The 1D periodic grating in PR was then patterned using 325 nm wavelength HeCd laser exposure in a Lloyd's mirror IL setup, where two coherent laser beams interfered to create periodic intensity pattern. Then, the 1D pattern was transferred to the underlying silicon substrate using O_2 and Cl_2 RIE. After etching, an RCA (the Radio Corporation of America) cleaning process was used to remove the organic contaminants on the substrate surface. The surfaces of the molds were then treated with silane to mitigate adhesion for the subsequent nanoimprint process.

For nanoimprint lithography, first a poly(dimethylsiloxane) stamp was cast from a silicon master structure (cured by 90 °C for 2 h) and subsequently used to nanoimprint into a grating structure on a spin-coated epoxy films (cured under UV exposure). The resultant grating structure was then UV-ozone treated for 30 min to improve wettability, and the perovskite precursor was spin coated on top of the sample using the above method. Finally, the fabricated devices were sealed in glovebox by UV-curable resin before testing.

Material and LED Device Characterization: XRD measurements were carried out with Rigaku Smartlab X-ray Diffractometer with a conventional Cu X-ray tube. Steady-state PL spectra of perovskite films were measured with an Edinburgh Instruments FS920 fluorimeter that was equipped with a 450 W Xe arc lamp for excitation source and a Peltier-cooled Hammamatsu R2658P photomultiplier tube (PMT). The excitation wavelength was 375 nm. Nanosecond TRPL spectra were collected on an LP 920 spectrometer from Edinburgh Instruments with the excitation of 390 nm. The UV–vis absorbance spectra were recorded on an UV–vis spectrophotometer (Lambda 750, PerkinElmer). SEM images of the perovskite films were collected in FEI Verios 460L. The *J–V–L* characterization was obtained by using Keithley 2400 sourcemeter.

ASE and Lasing Characterization: For ASE and lasing spectra measurements, samples were pumped by 400 nm pulsed laser which was obtained from second harmonic generation of the 800 nm 150 fs output from Quantronix Integra-C laser. The pulse width was 150 fs, the repetition was 1 kHz, and the spot size was 4.5 mm in diameter. Resulting emission was recorded by the charge-coupled device (CCD) spectrometer from Mightex Systems. All spectroscopy measurements were carried out in air.

GIWAXS: Films were spin-cast on silicon substrates in preparation for the GIWAXS measurements. GIWAXS was conducted on each sample in a He atmosphere at beamline 7.3.3 at the Advanced Light Source (ALS) in Lawrence Berkeley National Lab (LBNL).[52] The incident photon energy was 10 keV at an incident angle of 1° and the scattered photons were collected by a Pilatus 2M detector. Patterns were processed, corrected, analyzed, and colored in a modified NIKA package of Igor Pro.[53] A logarithmic color scale was used for each pattern. The software indexGIXS 2.0, CrystalMaker 10.2.2, and CrystalDiffract 6.7.3 were used to help index peaks in the GIWAXS patterns.[40]

TAS: Transient absorption data were collected using TAS setup. This setup was consisted of the spectrometer (Ultrafast Helios system) and amplified Ti:Saphhire laser. The output of amplified Ti:Saphhire laser provided 800 nm fundamental pulses at 1 kHz repetition rate which were split into two optical beams to generate pump and probe pulses. One fundamental beam was used to generate pump beam using an optical parametric amplifier system (Coherent Opera Solo). A white light/near-infrared probe was generated by focusing another fundamental beam into a flint glass. Pump and probe beams were focused on a sample and probe light was collected by a CCD device. The spectral detection region was 350–600 nm. The thin-film samples were prepared on glass substrates and encapsulated using UV curable glue before measurement. The instrument response function was ≈100 fs FWHM. The samples were excited with the excitation wavelength of 355 nm and the fractional change in transmission was detected in the probe range 350–600 nm at several time delays.

Supporting Information

Supporting Information is available from the Wiley Online Library or from the author.

Acknowledgements

The authors are thankful for the support from the National Science Foundation DMREF Program (NSF Award #1729383) and the UNC Research Opportunities Initiative Center for Hybrid Materials Enabled Electronic Technologies (CHMEET). The GIWAXS data were acquired at beamline 7.3.3 at the ALS in Lawrence Berkeley National Laboratory,[52] which is supported by the U.S. Department of Energy (no. DE-AC02-05CH11231). Experimental support was provided at the ALS by beamline scientists C. Zhu and A. Liebman-Pelaez. H.A. and S.S. are supported by UNC-GA Research Opportunity Initiative (ROI) grant. Work by C.-H.C. is supported by the National Science Foundation (NSF) grant CMMI#1552424. The part of the work (XRD and SEM) was performed in the Analytical Instrumentation Facility (AIF) at North Carolina State University, which is supported by the State of North Carolina and the National Science Foundation (award number ECCS-1542015). The AIF is a member of the North Carolina Research Triangle Nanotechnology Network (RTNN), a site in the National Nanotechnology Coordinated Infrastructure (NNCI).

Conflict of Interest

The authors declare no conflict of interest.

Keywords

amplified spontaneous emission, distributed-feedback lasers, energy funneling, light-emitting diodes, quasi-2D perovskites

Received: October 7, 2019
Revised: January 16, 2020

---

[1] G. Hodes, *Science* **2013**, *342*, 317.
[2] K. Lin, J. Xing, L. N. Quan, F. P. G. de Arquer, X. Gong, J. Lu, L. Xie, W. Zhao, D. Zhang, C. Yan, W. Li, X. Liu, Y. Lu, J. Kirman, E. H. Sargent, Q. Xiong, Z. Wei, *Nature* **2018**, *562*, 245.
[3] M. Saliba, S. M. Wood, J. B. Patel, P. K. Nayak, J. Huang, J. A. Alexander-Webber, B. Wenger, S. D. Stranks, M. T. Hörantner, J. T. Wang, R. J. Nicholas, L. M. Herz, M. B. Johnston, S. M. Morris, H. J. Snaith, M. K. Riede, *Adv. Mater.* **2016**, *28*, 923.
[4] Y. Cao, N. Wang, H. Tian, J. Guo, Y. Wei, H. Chen, Y. Miao, W. Zou, K. Pan, Y. He, H. Cao, Y. Ke, M. Xu, Y. Wang, M. Yang, K. Du, Z. Fu, D. Kong, D. Dai, Y. Jin, G. Li, H. Li, Q. Peng, J. Wang, W. Huang, *Nature* **2018**, *562*, 249.
[5] N. Wang, L. Cheng, R. Ge, S. Zhang, Y. Miao, W. Zou, C. Yi, Y. Sun, Y. Cao, R. Yang, Y. Wei, Q. Guo, Y. Ke, M. Yu, Y. Jin, Y. Liu, Q. Ding, D. Di, L. Yang, G. Xing, H. Tian, C. Jin, F. Gao, R. H. Friend, J. Wang, W. Huang, *Nat. Photonics* **2016**, *10*, 699.
[6] Z. Xiao, R. A. Kerner, L. Zhao, N. L. Tran, K. M. Lee, T.-W. Koh, G. D. Scholes, B. P. Rand, *Nat. Photonics* **2017**, *11*, 108.
[7] Z. Tan, R. S. Moghaddam, M. L. Lai, P. Docampo, R. Higler, F. Deschler, M. Price, A. Sadhanala, L. M. Pazos, D. Credgington, F. Hanusch, T. Bein, H. J. Snaith, R. H. Friend, *Nat. Nanotechnol.* **2014**, *9*, 687.
[8] B. Zhao, S. Bai, V. Kim, R. Lamboll, R. Shivanna, F. Auras, J. M. Richter, L. Yang, L. Dai, M. Alsari, X. She, L. Liang, J. Zhang, S. Lilliu, P. Gao, H. J. Snaith, J. Wang, N. C. Greenham, R. H. Friend, D. Di, *Nat. Photonics* **2018**, *12*, 783.
[9] Y. Zou, M. Ban, Y. Yang, S. Bai, C. Wu, Y. Han, T. Wu, Y. Tan, Q. Huang, X. Gao, T. Song, Q. Zhang, B. Sun, *ACS Appl. Mater. Interfaces* **2018**, *10*, 24320.
[10] G. Xing, N. Mathews, S. S. Lim, N. Yantara, X. Liu, D. Sabba, M. Grätzel, S. Mhaisalkar, T. C. Sum, *Nat. Mater.* **2014**, *13*, 476.
[11] P. Chhantyal, S. Naskar, T. Birr, T. Fischer, F. Lübkemann, B. N. Chichkov, D. Dorfs, N. C. Bigall, C. Reinhardt, *Sci. Rep.* **2018**, *8*, 3962.
[12] H. Nakanotani, S. Akiyama, D. Ohnishi, M. Moriwake, M. Yahiro, T. Yoshihara, S. Tobita, C. Adachi, *Adv. Funct. Mater.* **2007**, *17*, 2328.
[13] F. Deschler, M. Price, S. Pathak, L. E. Klintberg, D.-D. Jarausch, R. Higler, S. Hüttner, T. Leijtens, S. D. Stranks, H. J. Snaith, M. Atatüre, R. T. Phillips, R. H. Friend, *J. Phys. Chem. Lett.* **2014**, *5*, 1421.
[14] S. Chen, C. Zhang, J. Lee, J. Han, A. Nurmikko, *Adv. Mater.* **2017**, *29*, 1604781.
[15] Z. Li, J. Moon, A. Gharajeh, R. Haroldson, R. Hawkins, W. Hu, A. Zakhidov, Q. Gu, *ACS Nano* **2018**, *12*, 10968.
[16] A. Zhizhchenko, S. Syubaev, A. Berestennikov, A. V. Yulin, A. Porfirev, A. Pushkarev, I. Shishkin, K. Golokhvast, A. A. Bogdanov, A. A. Zakhidov, A. A. Kuchmizhak, Y. S. Kivshar, S. V. Makarov, *ACS Nano* **2019**, *13*, 4140.
[17] H. Zhang, Y. Wu, Q. Liao, Z. Zhang, Y. Liu, Q. Gao, P. Liu, M. Li, J. Yao, H. Fu, *Angew. Chem., Int. Ed.* **2018**, *57*, 7748.
[18] T. Ishihara, X. Hong, J. Ding, A. V. Nurmikko, *Surf. Sci.* **1992**, *267*, 323.
[19] L. N. Quan, M. Yuan, R. Comin, O. Voznyy, E. M. Beauregard, S. Hoogland, A. Buin, A. R. Kirmani, K. Zhao, A. Amassian, D. H. Kim, E. H. Sargent, *J. Am. Chem. Soc.* **2016**, *138*, 2649.
[20] M. Yuan, L. N. Quan, R. Comin, G. Walters, R. Sabatini, O. Voznyy, S. Hoogland, Y. Zhao, E. M. Beauregard, P. Kanjanaboos, Z. Lu, D. H. Kim, E. H. Sargent, *Nat. Nanotechnol.* **2016**, *11*, 872.
[21] G. Xing, B. Wu, X. Wu, M. Li, B. Du, Q. Wei, J. Guo, E. K. L. Yeow, T. C. Sum, W. Huang, *Nat. Commun.* **2017**, *8*, 14558.
[22] M. Li, Q. Gao, P. Liu, Q. Liao, H. Zhang, J. Yao, W. Hu, Y. Wu, H. Fu, *Adv. Funct. Mater.* **2018**, *28*, 1707006.
[23] M. Ban, Y. Zou, J. P. H. Rivett, Y. Yang, T. H. Thomas, Y. Tan, T. Song, X. Gao, D. Credgington, F. Deschler, H. Sirringhaus, B. Sun, *Nat. Commun.* **2018**, *9*, 3892.
[24] M. R. Leyden, S. Terakawa, T. Matsushima, S. Ruan, K. Goushi, M. Auffray, A. S. D. Sandanayaka, C. Qin, F. Bencheikh, C. Adachi, *ACS Photonics* **2019**, *6*, 460.
[25] H. Zhang, Q. Liao, Y. Wu, Z. Zhang, Q. Gao, P. Liu, M. Li, J. Yao, H. Fu, *Adv. Mater.* **2018**, *30*, 1706186.
[26] M. R. Leyden, T. Matsushima, C. Qin, S. Ruan, H. Ye, C. Adachi, *Phys. Chem. Chem. Phys.* **2018**, *20*, 15030.
[27] L. N. Quan, Y. Zhao, F. P. García de Arquer, R. Sabatini, G. Walters, O. Voznyy, R. Comin, Y. Li, J. Z. Fan, H. Tan, J. Pan, M. Yuan, O. M. Bakr, Z. Lu, D. H. Kim, E. H. Sargent, *Nano Lett.* **2017**, *17*, 3701.
[28] N. Yantara, A. Bruno, A. Iqbal, N. F. Jamaludin, C. Soci, S. Mhaisalkar, N. Mathews, *Adv. Mater.* **2018**, *30*, 1800818.
[29] H. Lee, H. Kim, H. Cho, W. Cha, Y. Hong, Y. Kim, A. Sadhanala, V. Venugopalan, J. S. Kim, J. W. Choi, C. Lee, D. Kim,

H. Yang, R. H. Friend, T. Lee, *Adv. Funct. Mater.* **2019**, *29*, 1901225.

[30] R. Wang, Y. Tong, A. Manzi, K. Wang, Z. Fu, E. Kentzinger, J. Feldmann, A. S. Urban, P. Müller-Buschbaum, H. Frielinghaus, *Adv. Opt. Mater.* **2018**, *6*, 1701311.

[31] M. Xiao, F. Huang, W. Huang, Y. Dkhissi, Y. Zhu, J. Etheridge, A. Gray-Weale, U. Bach, Y. B. Cheng, L. Spiccia, *Angew. Chem., Int. Ed.* **2014**, *53*, 9898.

[32] Y. Jo, K. S. Oh, M. Kim, K.-H. Kim, H. Lee, C.-W. Lee, D. S. Kim, *Adv. Mater. Interfaces* **2016**, *3*, 1500768.

[33] J. C. Hamill, J. Schwartz, Y. Loo, *ACS Energy Lett.* **2018**, *3*, 92.

[34] M. Yang, Z. Li, M. O. Reese, O. G. Reid, D. H. Kim, S. Siol, T. R. Klein, Y. Yan, J. J. Berry, M. F. A. M. van Hest, K. Zhu, *Nat. Energy* **2017**, *2*, 17038.

[35] J.-W. Lee, Z. Dai, C. Lee, H. M. Lee, T. Han, N. De Marco, O. Lin, C. S. Choi, B. Dunn, J. Koh, D. Di Carlo, J. H. Ko, H. D. Maynard, Y. Yang, *J. Am. Chem. Soc.* **2018**, *140*, 6317.

[36] R. Quintero-Bermudez, A. Gold-Parker, A. H. Proppe, R. Munir, Z. Yang, S. O. Kelley, A. Amassian, M. F. Toney, E. H. Sargent, *Nat. Mater.* **2018**, *17*, 900.

[37] J. Rivnay, S. C. B. Mannsfeld, C. E. Miller, A. Salleo, M. F. Toney, *Chem. Rev.* **2012**, *112*, 5488.

[38] J. Hu, I. W. H. Oswald, S. J. Stuard, M. M. Nahid, N. Zhou, O. F. Williams, Z. Guo, L. Yan, H. Hu, Z. Chen, X. Xiao, Y. Lin, Z. Yang, J. Huang, A. M. Moran, H. Ade, J. R. Neilson, W. You, *Nat. Commun.* **2019**, *10*, 1276.

[39] N. R. Venkatesan, J. G. Labram, M. L. Chabinyc, *ACS Energy Lett.* **2018**, *3*, 380.

[40] D. Smilgies, D. R. Blasini, *J. Appl. Crystallogr.* **2007**, *40*, 716.

[41] X. Yang, X. Zhang, J. Deng, Z. Chu, Q. Jiang, J. Meng, P. Wang, L. Zhang, Z. Yin, J. You, *Nat. Commun.* **2018**, *9*, 570.

[42] M. A. Omary, H. H. Patterson, in *Encyclopedia of Spectroscopy and Spectrometry*, 3rd ed. (Eds: J. C. Lindon, G. E. Tranter, D. W. Koppenaal), Academic Press, **2017**, pp. 636–653.

[43] A. Fieramosca, L. De Marco, M. Passoni, L. Polimeno, A. Rizzo, B. L. T. Rosa, G. Cruciani, L. Dominici, M. De Giorgi, G. Gigli, L. C. Andreani, D. Gerace, D. Ballarini, D. Sanvitto, *ACS Photonics* **2018**, *5*, 4179.

[44] B. Wallace, P. J. Atzberger, *PLoS One* **2017**, *12*, 1.

[45] J. B. Hoffman, R. Alam, P. V. Kamat, *ACS Energy Lett.* **2017**, *2*, 391.

[46] C. de Weerd, L. Gomez, H. Zhang, W. J. Buma, G. Nedelcu, M. V. Kovalenko, T. Gregorkiewicz, *J. Phys. Chem. C* **2016**, *120*, 13310.

[47] J. Even, L. Pedesseau, M.-A. Dupertuis, J.-M. Jancu, C. Katan, *Phys. Rev. B* **2012**, *86*, 205301.

[48] T. Ishihara, J. Takahashi, T. Goto, *Phys. Rev. B* **1990**, *42*, 11099.

[49] S. Liu, S. Ho, Y. Chen, F. So, *Chem. Mater.* **2015**, *27*, 2532.

[50] R. J. Noll, S. H. Macomber, *IEEE J. Quantum Electron.* **1990**, *26*, 456.

[51] Y. Jia, R. A. Kerner, A. J. Grede, A. N. Brigeman, B. P. Rand, N. C. Giebink, *Nano Lett.* **2016**, *16*, 4624.

[52] A. Hexemer, W. Bras, J. Glossinger, E. Schaible, E. Gann, R. Kirian, A. MacDowell, M. Church, B. Rude, H. Padmore, *J. Phys.: Conf. Ser.* **2010**, *247*, 012007.

[53] J. Ilavsky, *J. Appl. Crystallogr.* **2012**, *45*, 324.